

Operator product expansion for radial lattice quantization of 3D ϕ^4 theory

Venkitesh Ayyar¹, Richard C. Brower¹, George T. Fleming^{2,3,*}, Anna-Maria E. Glück^{4,3,†},
Evan K. Owen¹, Timothy G. Raben⁵, and Chung-I Tan⁶

¹*Department of Physics and Center for Computational Science, Boston University,
Boston, Massachusetts 02215, USA*

²*Fermi National Accelerator Laboratory, Batavia, Illinois 60510, USA*

³*Department of Physics, Sloane Laboratory, Yale University, New Haven, Connecticut 06511, USA*

⁴*Kirchhoff-Institut für Physik, Ruprecht-Karls-Universität Heidelberg, 69120 Heidelberg, Germany*

⁵*Department of Physics and Astronomy, Michigan State University, East Lansing, Michigan 48824, USA*

⁶*Brown Theoretical Physics Center and Department of Physics, Brown University,
Providence, Rhode Island 02912, USA*

 (Received 6 December 2023; accepted 7 February 2024; published 24 June 2024)

At its critical point, the three-dimensional lattice Ising model is described by a conformal field theory (CFT), the 3D Ising CFT. Instead of carrying out simulations on Euclidean lattices, we use the quantum finite elements method to implement radially quantized critical ϕ^4 theory on simplicial lattices approaching $\mathbb{R} \times S^2$. Computing the four-point function of identical scalars, we demonstrate the power of radial quantization by the accurate determination of the scaling dimensions Δ_ϵ and Δ_T as well as ratios of the operator product expansion coefficients $f_{\sigma\sigma\epsilon}$ and $f_{\sigma\sigma T}$ of the first spin-0 and spin-2 primary operators ϵ and T of the 3D Ising CFT.

DOI: [10.1103/PhysRevD.109.114518](https://doi.org/10.1103/PhysRevD.109.114518)

I. INTRODUCTION

Since the first discovery of critical opaqueness made by Andrews in the 19th century [1] and especially since Wilson's breakthrough formulation of the renormalization group (RG) framework for critical phenomena [2], the study of systems at criticality has fascinated physicists throughout the decades. The prototype of such a system with a continuous phase transition and the workhorse in studying critical phenomena is the Ising model. Despite its simplicity, it is of great physical relevance because universality guarantees that the critical Ising model shows the same behavior as encountered for critical transitions in e.g. uniaxial magnetic systems, fluids [3], and micellar systems [4].

Motivated by experimental measurements of the scaling behavior of physical quantities near criticality, past theoretical efforts to study the critical point of the Ising model had the main goal of calculating its critical exponents. As there is no analytic solution for the Ising model in $d \geq 3$, such calculations have to be performed using approximate and computational methods, the most prominent of those

including high-temperature expansions, field-theoretic methods such as the ϵ -expansion or nonperturbative methods based on approximate solutions of the RG-equations, as well as Monte Carlo simulations. For a review, see [5]. After the development of spin cluster algorithms [6,7], especially the latter method combined with finite-size scaling arguments yielded precise results for the critical exponents [5,8,9].

For comparison with experiments, it is sufficient to determine the critical exponents of the 3D Ising model. But from a theoretical point of view, the critical Ising model contains much more information. Following Polyakov's hypothesis [10], we expect the scale invariance of a system at criticality combined with Poincaré invariance to lead this critical system to be invariant under the conformal group $O(d+1, 1)$. Consequently, the physics of the critical 3D Ising model can be described by a conformal field theory (CFT), the 3D Ising CFT [11]. The local operator content of such a CFT is spanned by the so-called *primary operators* and their descendants, which are created by acting on the primaries with translation generators. The primary operators can be assigned spins and parity and, in the case of the 3D Ising CFT, include the leading 0^- -operator σ , the leading 0^+ -operator ϵ and the energy-momentum tensor T (2^+), as well as infinitely many subleading and higher-spin operators. As will be further explained in Sec. II, a CFT is characterized by two sets of quantities—the *scaling dimensions* $\Delta_{\mathcal{O}}$ and the *operator product expansion (OPE) coefficients* $f_{\mathcal{O}_1\mathcal{O}_2\mathcal{O}_3}$ for different primary operators \mathcal{O} of the

*gfleming@fnal.gov

†anna-maria.glueck@stud.uni-heidelberg.de

Published by the American Physical Society under the terms of the [Creative Commons Attribution 4.0 International license](https://creativecommons.org/licenses/by/4.0/). Further distribution of this work must maintain attribution to the author(s) and the published article's title, journal citation, and DOI. Funded by SCOAP³.

CFT. This CFT point of view on the critical Ising model has most prominently been taken by the conformal bootstrap method [12–14] to obtain extremely precise values for both scaling dimensions and OPE coefficients for several primary operators [15,16].

For (at least some of) the scaling dimensions, there is a mapping to the critical exponents, which have been thoroughly investigated with the traditional methods reviewed in [5]

$$\begin{aligned}\eta &= 2\Delta_\sigma - d + 2, \\ \nu &= 1/(d - \Delta_\epsilon), \\ \omega &= \Delta_{\epsilon'} - d.\end{aligned}\quad (1)$$

The OPE coefficients, however, are largely uninvestigated with these methods. With functional renormalization group methods, it was only recently possible to determine $f_{\sigma\sigma\epsilon}$ [17]. Moreover, $f_{\sigma\sigma\epsilon}$ and $f_{\epsilon\epsilon\epsilon}$ have been measured with traditional Monte Carlo methods on Euclidean lattices from three-point correlators [18,19] and from the scaling of two-point correlators [20,21] of the operators σ and ϵ .

However, as suggested by Cardy [22] in 1985, there is, in principle, a huge advantage by replacing the traditional toroidal Euclidean lattice approximation to \mathbb{R}^d with simulations on simplicial lattices convergent to the cylindrical $\mathbb{R} \times S^{d-1}$. This is an exact Weyl map of all CFT data to what is called *radial quantization* [23] with translations generated by the dilatation operator. The challenge [22] for $d > 2$ is to define the correct lattice action on the curved manifold. Recently, the *quantum finite elements (QFE)* [24] project has begun to address this by including lattice counter terms to improve the UV cutoff.

QFE tests began with ϕ^4 theory at the critical point in comparison with the minimal 2D Ising CFT on S^2 , accurately reproducing the exact results for the \mathbb{Z}_2 -odd scalar propagator and the scalar four-point amplitude [25] as well as examples of the \mathbb{Z}_2 -even sector in the fermionic representation [26] on S^2 . The next step was to apply the QFE to critical ϕ^4 theory on $\mathbb{R} \times S^2$ in order to compare to the 3D Ising CFT. The scalar propagator [27] was well-represented in the continuum limit with the scaling dimension Δ_σ determined to better than 10^{-2} agreement with the conformal bootstrap [15,16]. Here, we extend the QFE method to the scalar four-point amplitude of the 3D Ising CFT. As the lowest n -point function with a nontrivial operator product expansion, the four-point function provides a stringent test of whether we reach the CFT in the continuum limit with our QFE method. Moreover, it is a good quantity to show that the 3D Ising CFT is more than just a small perturbation from the Gaussian theory [28] presented in Sec. VI, as the scaling dimension for some operators like ϵ have been found to deviate significantly from their free values [15,16]. The present work is intended as a proof of concept to show that by fitting our lattice data

to the expected form from the continuum OPE for CFTs in radial quantization, we can extract scaling dimensions $\Delta_{\mathcal{O}}$ and OPE coefficients $f_{\sigma\sigma\mathcal{O}}$ of \mathbb{Z}_2 -even primary operators in the continuum limit. Preliminary results presented at LATTICE 2022 [29] are extended and finalized here to higher fidelity to assess the capabilities of our method.

In the conclusion, we discuss further improvements of the QFE method and make comparisons with results from the conformal bootstrap [13–16], which offer definitive tests for Monte Carlo simulations even for nonintegral theories. Moreover, there are recent successes in determining OPE coefficients using Hamiltonian methods on the fuzzy sphere [30,31]. While each method is complementary, comparisons may suggest improvement for them all.

II. N -POINT FUNCTIONS IN RADIALLY QUANTIZED CFTs

A. CFTs and radial quantization

At the Wilson-Fisher fixed point, 3D ϕ^4 theory is described by the 3D Ising CFT. d -dimensional CFTs are quantum field theories that are invariant under the conformal group $O(d+1, 1)$ of transformations that leave the metric invariant up to a Weyl rescaling [32]

$$g_{\mu\nu}(\mathbf{x}) \rightarrow g'_{\mu\nu}(\mathbf{x}') = \Lambda^2(\mathbf{x})g_{\mu\nu}(\mathbf{x}). \quad (2)$$

Thus, instead of considering the 3D Ising CFT on three-dimensional Euclidean space with metric,

$$ds_{\text{flat}}^2 = dr^2 + r^2 d\Omega^2 = \frac{r^2}{R^2} [dt^2 + R^2 d\Omega^2], \quad (3)$$

where $t = R \log(r/R)$, one can quantize the theory on $\mathbb{R} \times S^2$ with Weyl-rescaled metric

$$ds_{\text{cyl}}^2 = dt^2 + R^2 d\Omega^2 = \frac{R^2}{r^2} ds_{\text{flat}}^2. \quad (4)$$

n -point functions of scalar fields in flat space are then related to those on the cylinder via

$$\begin{aligned}\langle \sigma(r_1, \Omega_1) \sigma(r_2, \Omega_2) \cdots \rangle_{\text{flat}} \\ = \left(\frac{R}{r_1}\right)^{\Delta_\sigma} \left(\frac{R}{r_2}\right)^{\Delta_\sigma} \cdots \langle \sigma(t_1, \Omega_1) \sigma(t_2, \Omega_2) \cdots \rangle_{\text{cyl}}\end{aligned}\quad (5)$$

with Δ_σ the scaling dimension of scalar primary σ [33]. This choice of coordinates is called radial quantization and is often useful for scale-invariant theories as dilatations of r on \mathbb{R}^3 are mapped to shifts in cylinder time t . As will be explained in Sec. II C, the determination of CFT data is also extremely facilitated by radial quantization.

B. Conformal n -point functions

Due to the symmetries of CFTs, two-point functions of primary operators follow power laws [32],

$$\langle \mathcal{O}(x_1) \mathcal{O}(x_2) \rangle = \frac{C_{\mathcal{O}}}{|x_1 - x_2|^{2\Delta_{\mathcal{O}}}}. \quad (6)$$

Moreover, the OPE is exact, such that under the path integral, a product of two primaries can be replaced by a sum over “intermediate states” (schematically)

$$\mathcal{O}_i(x_1) \mathcal{O}_j(x_2) = \sum_k f_{\mathcal{O}_i \mathcal{O}_j \mathcal{O}_k} C(x_1 - x_2) \mathcal{O}_k(x_2), \quad (7)$$

with the OPE coefficients $f_{\mathcal{O}_i \mathcal{O}_j \mathcal{O}_k}$ as expansion coefficients. Thus, all n -point functions of a CFT can be expressed as functions of the scaling dimensions $\Delta_{\mathcal{O}}$ and the OPE coefficients $f_{\mathcal{O}_i \mathcal{O}_j \mathcal{O}_k}$ of conformal primaries \mathcal{O} . Moreover, all those quantities can be extracted by measuring different four-point functions.

In this work, we focus on the four-point function of four identical scalar primaries σ , which—when divided by the corresponding two-point functions—forms the amplitude $g(u, v)$. It is called the conformally invariant amplitude as any factors Eq. (5) from Weyl rescaling the metric equation (2) drop out. Thanks to the OPE, this amplitude can be expanded into a sum over the primaries \mathcal{O} of the CFT [34,35]:

$$g(u, v) \equiv \frac{\langle \sigma(x_1) \sigma(x_2) \sigma(x_3) \sigma(x_4) \rangle}{\langle \sigma(x_1) \sigma(x_2) \rangle \langle \sigma(x_3) \sigma(x_4) \rangle} \quad (8)$$

$$= 1 + \sum_{\mathcal{O}} f_{\sigma\sigma\mathcal{O}}^2 G_{\mathcal{O}}(\Delta_{\mathcal{O}}; u, v). \quad (9)$$

In this case, actually only the primaries \mathcal{O} with even spin and parity contribute because of the symmetries of the amplitude. The $G_{\mathcal{O}}$ are the so-called conformal blocks, functions of the scaling dimensions $\Delta_{\mathcal{O}}$ of primaries \mathcal{O} as well as the kinematic information encoded in the conformally invariant cross ratios u and v ,

$$\sqrt{u} = \frac{|x_1 - x_2| |x_3 - x_4|}{|x_1 - x_3| |x_2 - x_4|}, \quad \sqrt{v} = \frac{|x_1 - x_4| |x_2 - x_3|}{|x_1 - x_3| |x_2 - x_4|}. \quad (10)$$

In odd dimensions, there is no known analytic form of the conformal blocks. However, if we express the $G_{\mathcal{O}}$ as a function of the (also conformally invariant) quantities

$$\cosh(\tau) = \frac{1 + \sqrt{v}}{\sqrt{u}}, \quad \cos(\alpha) = \frac{1 - \sqrt{v}}{\sqrt{u}}, \quad (11)$$

they can be expanded in an absolutely convergent series in the Gegenbauer polynomials [36,37]:

$$G_{\mathcal{O}}(\tau, \alpha) = \sum_{n \in 2\mathbb{N}_0} e^{-(\Delta_{\mathcal{O}} + n)\tau} \sum_j B_{n,j}(\Delta_{\mathcal{O}}) C_j^{d/2-1}(\cos \alpha), \quad (12)$$

where in $d = 3$ dimensions the Gegenbauer polynomials correspond to the Legendre polynomials $C_j^{d/2-1}(\cos \alpha) = P_j(\cos \alpha)$. The j in the second sum is determined by the usual rules for the addition of angular momenta between the spin l of the primary \mathcal{O} and n ,

$$j \in \{\max(0, l - n), \dots, l + n\}, \quad (13)$$

and the $B_{n,j}$ are normalization coefficients. In three dimensions, they are normalized by

$$B_{0,j}(\Delta_{\mathcal{O}}) = 4^{\Delta_{\mathcal{O}}} \frac{l!}{(1/2)_l} \delta_{j,l}, \quad (14)$$

where $(\cdot)_l$ is the Pochhammer symbol. For their recursive calculation, we used the *Mathematica* Notebook provided with [37].

C. The antipodal scalar four-point function on $\mathbb{R} \times S^2$

We now consider the theory on $\mathbb{R} \times S^2$. On this manifold, the dilatation operator plays the role of the Hamiltonian and α and τ are the natural coordinates in which the symmetries of the four-point function are manifest even for theories away from the critical point. If we measure the four-point function on this manifold with $x_i = (t_i, \mathbf{n}_i)$, $i \in \{1, 2, 3, 4\}$ placed such that they lie pairwise at identical times, $t_1 = t_2$ and $t_3 = t_4$, and on antipodal points of S^2 , $\mathbf{n}_1 = -\mathbf{n}_2$ and $\mathbf{n}_3 = -\mathbf{n}_4$ (see Fig. 1), we have [27]

$$\mathbf{n}_1 \cdot \mathbf{n}_4 \equiv \cos(\theta) = \cos(\alpha), \quad \cosh(t) = \cosh(\tau) \quad (15)$$

such that we can directly measure

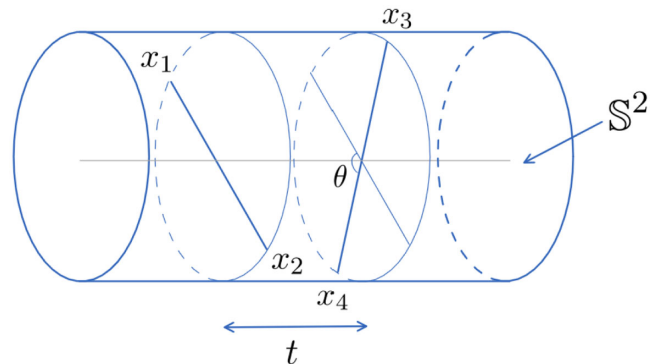


FIG. 1. Schematic illustration of the antipodal frame on $\mathbb{R} \times S^2$ in which we calculate the four-point function.

$$g(t, \cos \theta) = 1 + \sum_{\mathcal{O}} f_{\sigma\sigma\mathcal{O}}^2 \sum_{n \in 2\mathbb{N}_0} e^{-(\Delta_{\mathcal{O}}+n)t} \times \sum_j B_{n,j}(\Delta_{\mathcal{O}}) P_j(\cos \theta). \quad (16)$$

This is the big advantage of doing lattice calculations in radial quantization compared to usual Euclidean lattices. Now $g(t, \cos \theta)$ has the form of a partial wave expansion in the chosen antipodal frame

$$g(t, \cos \theta) = 1 + \sum_j c_j(t) P_j(\cos \theta) \quad (17)$$

with expansion coefficients

$$c_j(t) = \sum_{\mathcal{O}} f_{\sigma\sigma\mathcal{O}}^2 \sum_{\substack{n \in 2\mathbb{N}_0 \\ n \geq |j-l|}} B_{n,j}(\Delta_{\mathcal{O}}) e^{-(\Delta_{\mathcal{O}}+n)t} \quad (18)$$

so that each expansion coefficient consists of infinite towers of exponentials for all even parity and even spin primaries. By fitting these expansion coefficients, we can extract the quantities $\Delta_{\mathcal{O}}$ and $f_{\sigma\sigma\mathcal{O}}$.

III. RADially QUANTIZING THE 3D ISING CFT WITH QUANTUM FINITE ELEMENTS

In Refs. [25,27], Brower *et al.* succeeded at radial lattice quantization of ϕ^4 theory. For that, they approximated S^2 via a series of simplicial lattices as shown in Fig. 2.

Starting from an icosahedron, its edges are first subdivided into L equal pieces, thereby introducing a finer triangulation. Subsequently, the $N = 10L^2 + 2$ vertices are projected onto the sphere. Using the finite element method, the classical action can then be discretized on this simplicial complex [27]:

$$S = \frac{1}{2} \sum_{t,x} \sum_{y \in (x,y)} \frac{l_{xy}^*}{l_{xy}} (\tilde{\phi}_{t,x} - \tilde{\phi}_{t,y})^2 + \frac{a^2}{4R^2} \sqrt{\tilde{g}_x} \tilde{\phi}_{t,x}^2 + \sqrt{\tilde{g}_x} \left[\frac{a^2}{a_7^2} (\tilde{\phi}_{t,x} - \tilde{\phi}_{t+1,x})^2 + m_0^2 \tilde{\phi}_{t,x}^2 + \lambda_0 \tilde{\phi}_{t,x}^4 \right], \quad (19)$$

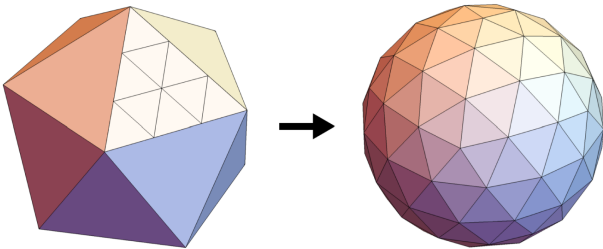


FIG. 2. Construction of the simplicial lattice for refinement $L = 3$.

where we sum over $x \in \{1, 2, \dots, N\}$ on each sphere and $t \in \{1, 2, \dots, L_t\}$ along the cylinder with periodic boundary conditions. Here, $\tilde{\phi}_{t,x}$ is the dimensionless field, m_0^2 and λ_0 the dimensionless mass and coupling. a and a_t are the average lattice spacings on the sphere and along the cylinder, respectively, and a is related to the radius R of the sphere via

$$a^2/R^2 = \frac{8\pi}{\sqrt{3}N} = \frac{8\pi}{\sqrt{3}(10L^2 + 2)}. \quad (20)$$

The bare speed of light a/a_t is set to one, though it is renormalized by interactions. For further details on the construction of this action as well as on how the dimensions of the quantities are restored, see Refs. [25,27].

While the position-dependent finite element weights l_{xy}^*/l_{xy} and $\sqrt{\tilde{g}_x}$ ensure the convergence of the action in Eq. (19) to the spherically symmetric classical continuum theory [25], Brower *et al.* found that for the quantum theory, they introduce fluctuations in the effective cutoff that are amplified by UV divergences, preventing convergence to the spherically symmetric quantum continuum theory [27]. To compensate for these quantum UV defects, perturbative counterterms, the so-called quantum finite elements, were introduced to the lattice action:

$$S_{QFE} = S - \sum_{t,x} \sqrt{\tilde{g}_x} (6\lambda_0 \delta G_{t,x} - 24\lambda_0^2 \delta G_{t,x}^{(3)}) \tilde{\phi}_{t,x}^2, \quad (21)$$

where $\delta G_{t,x}$ and $\delta G_{t,x}^{(3)}$ are calculated numerically from the free lattice propagator $G_{t,x;t',y}$ via

$$\delta G_{t,x} \equiv G_{t,x;t,x} - \frac{1}{N} \sum_{x'=1}^N \sqrt{\tilde{g}_{x'}} G_{t,x';t,x'}, \quad (22)$$

$$\delta G_{t,x}^{(3)} \equiv \sum_{t',y} \sqrt{\tilde{g}_y} \left(G_{t,x;t',y}^3 - \frac{1}{N} \sum_{x'=1}^N \sqrt{\tilde{g}_{x'}} G_{t,x';t',y}^3 \right). \quad (23)$$

In order to tune this QFE action to the Ising critical surface, the Binder cumulant was studied for fixed $\lambda_0 = 0.2$, finding $m_0^2 = -\mu_0^2 = -0.27018(4)$ as the critical coupling. With the parameters tuned to these values, the study of the scalar two-point function carried out in [27] suggests that we reach the 3D Ising CFT in the continuum limit $a/R \rightarrow 0$. In the following, we will fix the bare parameters to these values for our analysis of the interacting theory.

IV. CALCULATING AND FITTING THE ANTIPODAL LATTICE FOUR-POINT FUNCTION

To compute the antipodal scalar four-point function on the lattice, we used our QFE action (21) and carried out

Monte Carlo simulations with the Brower-Tamayo cluster algorithm [38] combined with Metropolis [39] and overrelaxation [40–43]. After some initial equilibration sweeps, \mathcal{O} (volume) four-point function configurations of our scalar lattice fields $\tilde{\phi}$ were sampled in each sweep along with the corresponding equal-time two-point functions to obtain $g(u, v)$ as in Eq. (8). Subsequently, we projected onto Legendre polynomials to obtain the expansion coefficients $c_j(t)$ in Eq. (12). Note that for finite lattice spacing, the lattice operator $\tilde{\phi}$ does not exactly correspond to the primary σ as in Eq. (12) but it is a mixture of all \mathbb{Z} -even scalar primaries of the CFT. However, as $a/R \rightarrow 0$, the contribution of operators other than σ go to zero.

Such simulations were carried out for different lattice refinements $L \in \{24, 28, 32, 36, 40, 44, 48, 56, 64\}$ in order to take the continuum limit later by sending $L \rightarrow \infty$, corresponding to $a/R \rightarrow 0$. We performed $N = 8000$ independent simulations for $L = 24$, $N = 1600$ for $32 \leq L \leq 56$, and $N = 800$ for $L = 64$. The resulting data is freely available in the Zenodo repository associated with this project [44]. For $L = 64$, the measured expansion coefficients up to $j = 20$ are shown in Fig. 3 with the error bars determined by the statistical error from averaging over the N independent runs. This figure illustrates that even for the L -value with the least amount of statistics, we have several timeslices of good data up until high j , such that it should in principle be possible to extract information about high-spin operators.

And in fact, by simply fitting unconstrained sets of exponentials to the different c_j , we could extract five exponentials for $j = 0$, and even for $j = 10$ we could fit up to three exponentials. However, the statistics did not allow, especially for the higher j , to always resolve the contribution from different primaries. For example, in the case of $j = 2$, we expect from Eq. (18) and the bootstrap

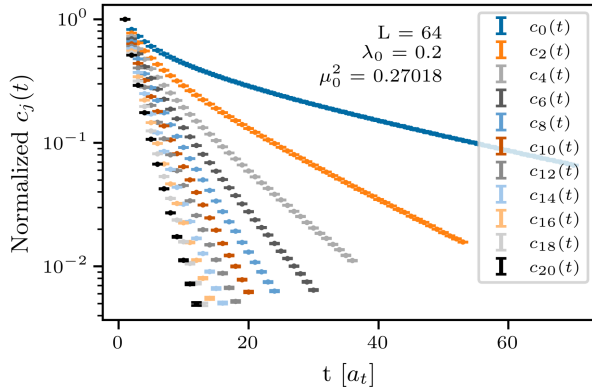


FIG. 3. Monte Carlo results for the four-point function expansion coefficients $c_j(t)$ from $N = 800$ independent runs with statistical errors. The coefficients are plotted for a t -range such that the relative error of the effective mass does not exceed $\Delta m_{\text{eff}}/m_{\text{eff}} \leq 0.125$.

TABLE I. Conformal bootstrap values for scaling dimensions and OPE coefficients of conformal primaries $\epsilon, T, \epsilon',$ and T' [15,16].

Operator \mathcal{O} (l^p)	$\Delta_{\mathcal{O}}$	$f_{\sigma\sigma\mathcal{O}}$
ϵ (0^+)	1.41265(36)	1.05185(12)
ϵ' (0^+)	3.82951(61)	0.05304(16)
T (2^+)	3	0.32613776(45)
T' (2^+)	5.499(17)	0.01054(10)

results in Table I that the leading exponential $\propto e^{-\Delta_T t}$ involves the scaling dimension Δ_T of the energy-momentum tensor T with $\ell = 2$, while the next-lowest exponential $\propto e^{-(\Delta_{\epsilon}+2)t}$ should stem from the $\ell = 0$ operator ϵ . To be able to resolve these two contributions at $L = 64$ without having to introduce additional constraints in the fitting parameters such as Eq. (18), we would likely have to increase the statistics by a factor 9–16, which is computationally not feasible as already the $N = 800$ runs took $\mathcal{O}(6 \times 10^5)$ hours of computing time on single cores on the BU shared computing cluster.

Thus, instead of fitting each c_j independently with unconstrained exponentials, we analyzed the Monte Carlo data by fitting the c_j simultaneously for different j with much more constrained functions based on the expansion Eq. (18). This has the advantage that adding a new primary operator \mathcal{O} to the fit only introduces two new fit parameters in total, namely $f_{\sigma\sigma\mathcal{O}}$ and $\Delta_{\mathcal{O}}$, while describing (in principle infinite) towers of exponentials for each c_j . The scaling dimension and OPE coefficients of a spin- l operator are then mainly determined by the operator’s contribution to c_ℓ while appropriately contributing to higher-order terms in c_j with $l \neq j$. Overall, this procedure improves convergence and helps resolve the different contributions.

Of course, strictly speaking, Eq. (18) is only true in the continuum limit as our finite lattice spacing breaks conformal invariance. However, we still performed fits based on the form of Eq. (18) because we expect that if a/R is small enough, the corrections due to the breaking of lattice spacing can be absorbed into corrections to our fit parameters that vanish as $a/R \rightarrow 0$.

In the present proof of principle, we focused on simultaneous fits to c_0 and c_2 , for which the leading contributions come from the primaries ϵ (0^+) and the energy-momentum tensor T (2^+), respectively. Furthermore, we included the first subleading operators for each ℓ , namely ϵ' (0^+) and T' (2^+) in our fits. We truncated the sums of exponentials at $n_{\text{max}} = 20$ for ϵ and correspondingly lower values for the other operators such that the largest exponents are of the same order of magnitude. With these truncations, Eq. (18) yields the following fit functions for $c_0(t)$ and $c_2(t)$ (in terms of the lattice “time” t)

$$\begin{aligned}
 c_0^{\text{fit}}(t) = & \sum_{n=0}^{n_{\text{max}}} f_{\sigma\sigma\epsilon}^2 B_{n,0}(\Delta_\epsilon) e^{-(\Delta_\epsilon+n)t a_t/R} \\
 & + \sum_{n=0}^{n_{\text{max}}-2} f_{\sigma\sigma\epsilon'}^2 B_{n,0}(\Delta_{\epsilon'}) e^{-(\Delta_{\epsilon'}+n)t a_t/R} \\
 & + \sum_{n=2}^{n_{\text{max}}-4} f_{\sigma\sigma T'}^2 B_{n,0}(\Delta_{T'}) e^{-(\Delta_{T'}+n)t a_t/R} \\
 & + (t \rightarrow L_t - t), \tag{24}
 \end{aligned}$$

$$\begin{aligned}
 c_2^{\text{fit}}(t) = & \sum_{n=0}^{n_{\text{max}}-2} f_{\sigma\sigma T}^2 B_{n,2}(\Delta_T) e^{-(\Delta_T+n)t a_t/R} \\
 & + \sum_{n=0}^{n_{\text{max}}-4} f_{\sigma\sigma T'}^2 B_{n,2}(\Delta_{T'}) e^{-(\Delta_{T'}+n)t a_t/R} \\
 & + \sum_{n=2}^{n_{\text{max}}} f_{\sigma\sigma\epsilon}^2 B_{n,2}(\Delta_\epsilon) e^{-(\Delta_\epsilon+n)t a_t/R} \\
 & + \sum_{n=2}^{n_{\text{max}}-2} f_{\sigma\sigma\epsilon'}^2 B_{n,2}(\Delta_{\epsilon'}) e^{-(\Delta_{\epsilon'}+n)t a_t/R} \\
 & + (t \rightarrow L_t - t), \tag{25}
 \end{aligned}$$

where the quantities $\Delta_{\mathcal{O}}$ and $f_{\sigma\sigma\mathcal{O}}^2$ are taken as the fit parameters. Note that we did not include contributions from the energy-momentum tensor T to $c_0(t)$ because for the theoretical continuum value $\Delta_T = 3$, all $B_{n,0}(3)$ vanish. In order to convert the lattice time of our data, which is given in units of a_t , to the time on $\mathbb{R} \times S^2$ in Eq. (18), which after the Weyl transform has units of R , we included factors a_t/R in the exponentials. This can be written as $a_t/R = a/(Rc_R)$ where a/R is known from Eq. (20) and c_R is the renormalized speed of light $c_R = a/a_t$. c_R was determined nonperturbatively in [27], yielding $c_R = 0.996$. Furthermore, to take into account wraparound the effects due to the periodicity along the cylinder to leading order, we added for each exponential in our fit function the same term with t substituted by $L_t - t$.

The light blue curves in Fig. 4 show the functions Eqs. (24) and (25) plotted with the bootstrap values for $\Delta_{\mathcal{O}}$ and $f_{\sigma\sigma\mathcal{O}}^2$, alongside our lattice data for $L = 64$. Comparison of these theoretical continuum curves with our lattice data shows apparent consistency, justifying our use of fit functions of this form. The other curves illustrate how the fit functions change depending on how many operators and n are included. Evidently, the operators ϵ and T are most influential while including the subleading ϵ' and T' only slightly shift the theoretical curve, mostly at low- t values. However, including these operators in fits decreased excited state contamination of the fit parameters for the leading operators and significantly increased the model probability of our fits, which we determined using the Akaike information criterion as described in [45]. Including

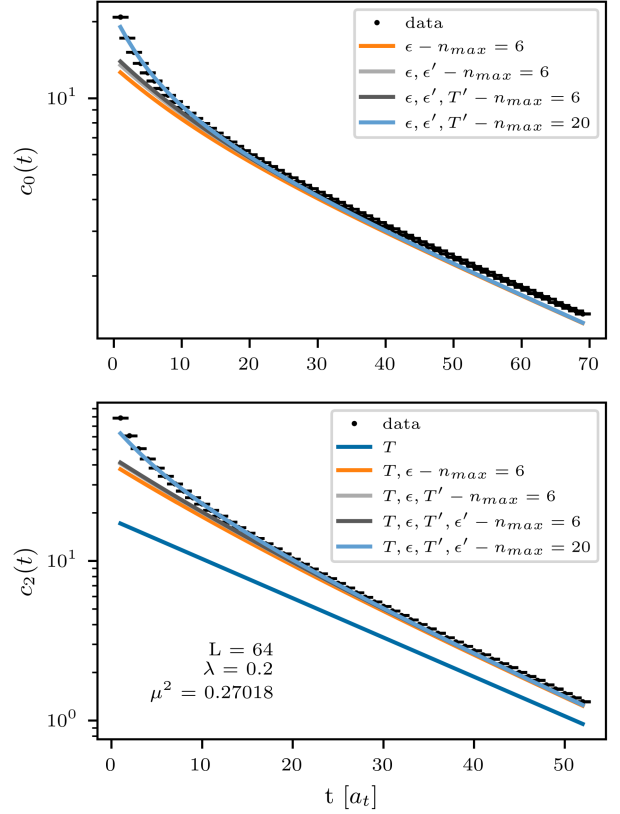


FIG. 4. Lattice data for c_0 and c_2 at a refinement of $L = 64$ compared to theoretical curves based on truncations of Eq. (18). For each curve, we include another primary operator contribution, corresponding to a new line in Eqs. (24) and (25), or a higher n_{max} . The light blue curve corresponds to the function we used for the fits in our analysis, including operators ϵ , ϵ' , T , and T' with $n_{\text{max}} = 20$. Note that these are not fits to the data but theoretical curves with the bootstrap values as scaling dimensions and OPE coefficients.

even higher order operators like ϵ'' led to either unconstrained or unphysical fit parameters, however. Thus, for simultaneous fits of c_0 and c_2 , we determined the fits including ϵ , ϵ' , T , and T' [Eqs. (24) and (25)] to be optimal.

Because of the truncations and approximations made in our fit functions, we do not expect them to describe our data within the entire t -range. Thus, we performed a model-averaging procedure as described in [45] in order to determine a reasonable range of minimal time slices ($t_0^{\text{min}}, t_2^{\text{min}}$). For each value of L , the fitting procedure can then be summarized as follows:

- (i) First, we performed simultaneous fits to $c_0(t)$ and $c_2(t)$ with the respective fit functions Eqs. (24) and (25) with fixed maximal time slices ($t_0^{\text{max}}, t_2^{\text{max}}$) and all possible combinations of starting times ($t_0^{\text{min}}, t_2^{\text{min}}$). Figure 4 suggested the use of the bootstrap values listed in Table I as initial guesses for our fit parameters to speed up the convergence of the nonlinear fitting procedure. However, we ensured that there is no dependence of our results on the

initial guesses by repeating the fits with the first-fit results as initial guesses and with checks perturbing these initial guesses. (t_0^{\max}, t_2^{\max}) were chosen such that the relative error of the effective mass for c_0 and c_2 never exceeded 12.5%. The simultaneous fits were carried out with the least squares method using the L-BFGS-B optimization algorithm implemented in `scipy` [46].

- (ii) Then, we calculated the model probabilities for all fits with the Akaike criterion according to [45].
- (iii) Thereafter, we discarded fits with unphysical [47] or unconstrained parameters (i.e. parameters with errors higher than 50%) as well as fits with (t_0^{\min}, t_2^{\min}) far from the values with highest model probability. After eliminating these fits, we renormalized the model probability.
- (iv) For each fit parameter, we lastly computed a weighted average over all fits with renormalized model probability higher than 0.1%.

The results of the individual fits used in calculating the final model-averaged values for each L are available in the Zenodo repository associated with this project [44].

V. RESULTS

The model-averaged fit results for the scaling dimensions and OPE coefficients of the leading operators are shown in Fig. 5 as functions of the dimensionless lattice spacing a/R . The errors were calculated from the covariances of the fits according to Eq. (17) in [45]. Thus, they do not capture possible systematic errors in the setup of the QFE framework.

If we compare our lattice results to the values obtained by the conformal bootstrap (shown in Table I and plotted as black dotted lines), it is apparent that Δ_ϵ , $f_{\sigma\sigma\epsilon}^2$, and Δ_T trend towards the continuum bootstrap values as $a/R \rightarrow 0$. Only $f_{\sigma\sigma T}^2$, the OPE coefficient associated with the energy-momentum tensor, does not show such a clear trend.

For a quantitative comparison, we had to extrapolate our lattice results to the continuum limit $a/R \rightarrow 0$. In Appendix B, we performed a finite-size scaling analysis of $g(u, v)$, yielding that to leading order, the squared OPE coefficients and scaling dimensions approach their continuum values with the leading power of $(a/R)^{\Delta_\epsilon - 3} \approx (a/R)^{0.83}$. To extrapolate our data to the continuum, we therefore fit our lattice results with functions of this form. Moreover, in the spirit of Taylor series approximations to

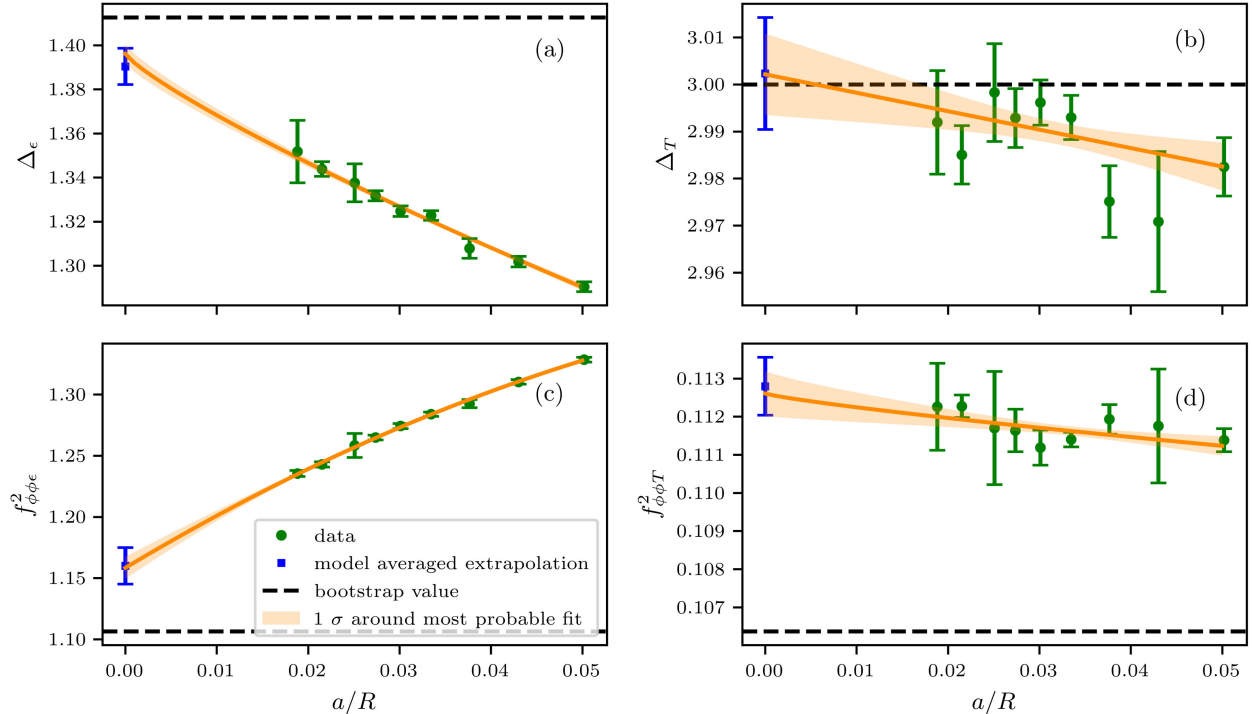


FIG. 5. Model-averaged fit results (green dots) for the scaling dimensions and OPE coefficients of the leading operators ϵ and T as a function of the lattice spacing. We have performed extrapolations to $a/R \rightarrow 0$ of different functional forms (26)–(28) and included different ranges of a/R . The values shown as blue squares at $a/R = 0$ correspond to the continuum results obtained after model averaging all different extrapolation fits. For each quantity, we also show the extrapolation fit with the highest model probability in orange; in (a) and (d), this is the finite-size scaling based fit, for (b) it is the linear extrapolation, and for (c) the quadratic fit, always including all data points. For comparison, the continuum bootstrap values are shown as dashed black lines.

TABLE II. Extrapolation results. We show the continuum values obtained with the finite-size scaling based fits including all data points, the results from the fits with the highest model probability, and the model averaged extrapolations for all quantities that are also plotted in Figs. 5–8. These values are compared to those obtained from the conformal bootstrap [15,16], and in the last column, we show the deviation of the model-averaged extrapolation values to the bootstrap results with respect to the statistical and fitting errors of our lattice results.

Quantity	Bootstrap	FSS fit	Fit with highest p_{model}	Fit model average	Deviation (σ)
Δ_ϵ	1.41265(36)	1.3961(46)	1.3961(46)	1.3905(83)	2.7
$f_{\sigma\sigma\epsilon}^2$	1.10639(26)	1.1625(31)	1.1583(91)	1.160(15)	3.6
Δ_T	3 (exact)	3.005(11)	3.0021(86)	3.002(12)	0.2
$f_{\sigma\sigma T}^2$	0.10636583(30)	0.11261(58)	0.11261(58)	0.11280(76)	8.5
$\Delta_{\epsilon'}$	3.82951(61)	3.82(24)	3.74(20)	3.78(27)	0.2
$f_{\sigma\sigma\epsilon'}^2$	0.0028102(59)	0.0020(24)	0.0027(20)	0.0028(29)	0.02
$C_T/C_T^{(\text{free})}$	0.946543(42)	0.896(10)	0.8961(81)	0.896(11)	3.9
$f_{\sigma\sigma\epsilon}^2/f_{\sigma\sigma T}^2$	10.4017(24)	10.312(79)	10.19(12)	10.30(16)	0.6
$C_T/C_T^{(\text{free})} \cdot f_{\sigma\sigma\epsilon}^2/\Delta_\epsilon^2$	0.52478(30)	0.5219(81)	0.5219(81)	0.528(16)	0.2

the true scaling form, we performed linear fits as well as fits including a linear and a quadratic term. Thus, the different fit functions we used for the continuum extrapolations are

$$f_{\text{FSS}} = c_1 \left(\frac{a}{R} \right)^{0.83} + c_0, \quad (26)$$

$$f_{\text{linear}} = c_1 \left(\frac{a}{R} \right) + c_0, \quad (27)$$

$$f_{\text{quadratic}} = c_2 \left(\frac{a}{R} \right)^2 + c_1 \left(\frac{a}{R} \right) + c_0. \quad (28)$$

Initially, we had also considered fits to general power laws, $f_{\text{power}} = c_1 \left(\frac{a}{R} \right)^{c_2} + c_0$. However, our statistics were not good enough to constrain all fit parameters. Similar problems arose for the quadratic fit, as the only quantity for which such fits could be constrained was $f_{\sigma\sigma\epsilon}^2$ due to its small error bars. Thus, $f_{\sigma\sigma\epsilon}^2$ is the only quantity for which we included such quadratic fits in determining our extrapolation results.

To account for the fact that for high a/R (low L) we might not be close enough to the continuum for our OPE-based fit functions to be applicable, we also carried out all extrapolating fits excluding the first one or two data points taken at the lowest lattice refinements ($L = 24$ and $L = 28$). Subsequently, we used model averaging again to weigh the extrapolated values of Δ_ϵ , Δ_T , $f_{\sigma\sigma\epsilon}^2$, and $f_{\sigma\sigma T}^2$ for the different fits by their model probability. Performing this procedure, we saw that in general, the model probability decreased the more low- L data points we excluded. Moreover, we note that the f_{FSS} fit to all data points was among the two extrapolations with the highest model probability for all quantities.

In Fig. 5, the most probable extrapolation fit (orange) as well as the model-averaged continuum extrapolation values (blue) are shown for the scaling dimensions and OPE

coefficients of the leading operators. The quantitative results of our extrapolations are given in Table II. It is apparent that the relative errors of our lattice results are significantly higher for the quantities associated with the $\ell = 2$ operator T compared to the leading $\ell = 0$ operator ϵ due to fact that we have better statistics for c_0 , in which T does not appear, than for c_2 . With these relatively high error bars, all of our extrapolations for Δ_T (and, thus, in particular the model-averaged extrapolation) are in good agreement with the exact value $\Delta_T = 3$. For Δ_ϵ , the model-averaged extrapolation is also just in agreement with the bootstrap value with a deviation of 2.7σ , even with just taking into account statistical and fitting errors.

Our continuum extrapolations of $f_{\sigma\sigma\epsilon}^2$ and $f_{\sigma\sigma T}^2$, however, are significantly higher than the respective bootstrap values. Given that the value of the OPE coefficients could be sensitive to our normalization choice Eq. (14) for the conformal blocks, we can explore the sensitivity to this potential source of systematic error by studying the ratio of the OPE coefficients $f_{\sigma\sigma\epsilon}^2$ and $f_{\sigma\sigma T}^2$ in Fig. 6, for which we performed the same extrapolation procedure as for the other quantities. If we take this ratio, all of our extrapolations are in 1σ agreement with the bootstrap value. This suggests that the normalization of conformal blocks at finite lattice discretization L warrants further study.

So far, we have only focused on the fit results for the quantities associated with the leading operators ϵ and T as these have the most signal and the least excited state contamination. To demonstrate that our method also works for the subleading operators, Fig. 7 shows our results for $\Delta_{\epsilon'}$ and $f_{\sigma\sigma\epsilon'}^2$, along with extrapolations to $a/R \rightarrow 0$. The error bars for those quantities are even larger than for Δ_T but the extrapolations show agreement with the bootstrap values. Here, we also do not have the issue of a deviation of the OPE coefficient from the bootstrap value as the extrapolated value for $f_{\sigma\sigma\epsilon'}^2$ has an error of 100%. To get more precise and reliable results for quantities associated

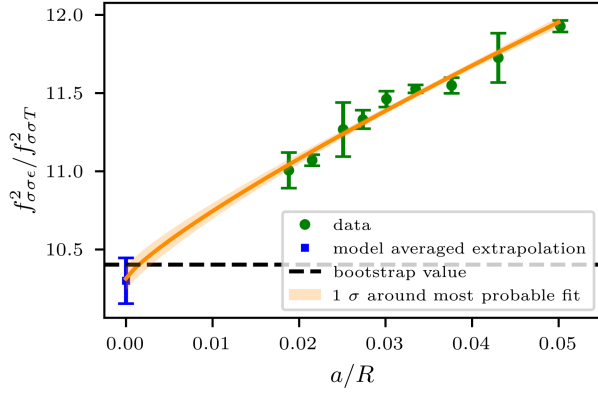


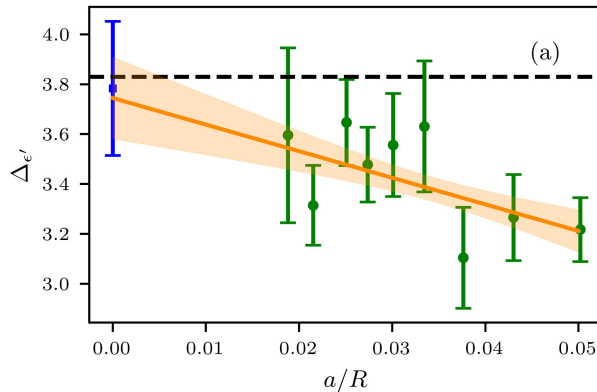
FIG. 6. Ratio of the model-averaged fit results for the OPE coefficients of the leading operators ϵ and T (green dots) as a function of the lattice spacing. We have performed extrapolations to $a/R \rightarrow 0$ according to (26) and (27) over different a/R -ranges. The extrapolation with the highest model probability is the finite-size scaling based fit using the lattice data for $L \geq 28$, shown in orange. The blue square at $a/R = 0$ represents the continuum value obtained after model averaging all extrapolations. For comparison, the continuum bootstrap value is shown as a dashed black line.

with ϵ' and T' , we would have to improve the statistics and go to even higher L in order to be able to include even more operators in our fits to reduce the excited state contamination of these quantities.

Lastly, we want to use our lattice results to determine the central charge of the 3D Ising CFT, which can be calculated via

$$C_T = \frac{\Delta_\sigma^2 \Delta_T^2}{16 f_{\sigma\sigma T}^2}. \quad (29)$$

Our results for the central charge relative to the free value $C_T^{(\text{free})} = 3/2$ can be seen in Fig. 8(a), where we use our lattice



values for Δ_T and $f_{\sigma\sigma T}^2$ to calculate C_T at different L . For Δ_σ we used our continuum value obtained in [27]. Because our continuum extrapolation for $f_{\sigma\sigma T}^2$ is significantly too high, it is not surprising that the extrapolation procedure performed for the central charge yields a continuum value that is significantly lower than the bootstrap value.

If we, however, take an appropriate ratio again, multiplying $C_T/C_T^{(\text{free})} \propto \Delta_T^2/f_{\sigma\sigma T}^2$ by $f_{\sigma\sigma\epsilon}^2/\Delta_\epsilon^2$, the extrapolation yields a continuum value in good agreement with the bootstrap [see Fig. 8(b)].

VI. FREE CFT ANALYSIS OF LATTICE ERRORS

Errors in the Monte Carlo simulations come from several sources: The statistical Monte Carlo sampling, possible systematic errors with a nonuniversal form of the action, and the finite lattice errors that need to be removed by extrapolating to infinite lattice volume in the IR and zero lattice spacing for the UV cutoff.

Clearly, the finite lattice errors can easily be evaluated for the exact free scalar CFT, for which we can calculate the four-point amplitude on the same lattices as in our current ϕ^4 simulations for the interacting theory. The comparison may be especially revealing here since the 3D Ising CFT is in some ways a small perturbation of the free CFT exploited in the epsilon expansion ($\epsilon = 4 - d$).

For the free theory, the exact continuum amplitude of the four-point function as in Eq. (8)

$$g^{(\text{free})}(u, v) = 1 + \frac{2}{(2 \cosh(t) - 2 \cos(\theta))^{\Delta_\sigma^{(\text{free})}}} + \frac{2}{(2 \cosh(t) + 2 \cos(\theta))^{\Delta_\sigma^{(\text{free})}}} \quad (30)$$

is a sum over pairs of two-point functions expressed in our radial coordinates

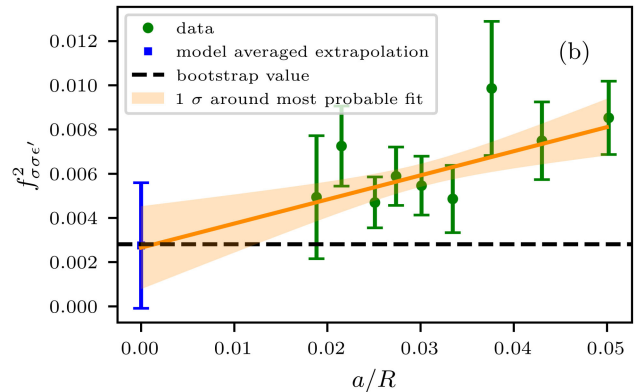


FIG. 7. Model-averaged fit results for the scaling dimension and OPE coefficient of the subleading $\ell = 0$ operator ϵ' (green dots) as a function of the lattice spacing. We have performed extrapolations to $a/R \rightarrow 0$ according to (26) and (27) over different a/R -ranges. The extrapolations with the highest model probability are linear fits using the lattice data for all a/R , shown in orange. The blue squares at $a/R = 0$ represent the continuum values obtained after model averaging all extrapolations. For comparison, the continuum bootstrap values are shown as dashed black lines.

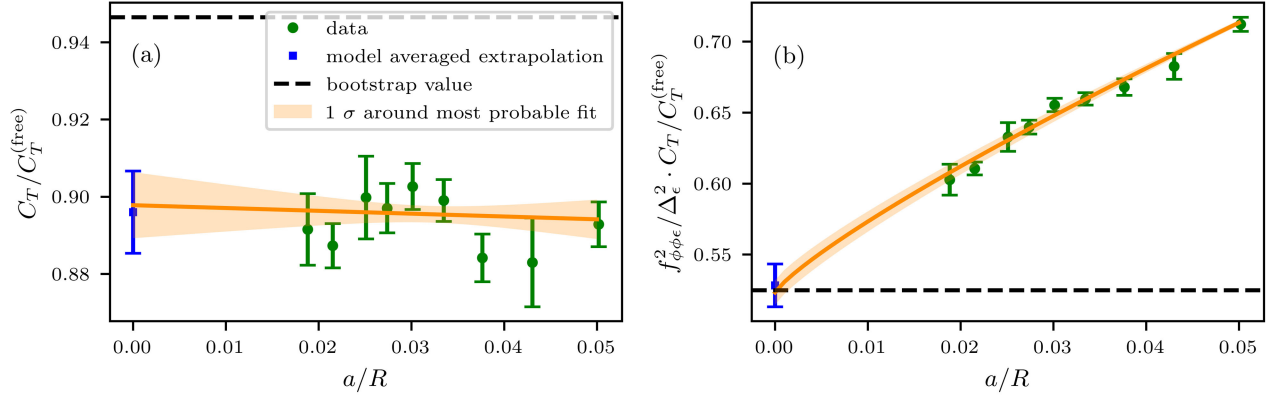


FIG. 8. (a) Central charge (green dots) in relation to $C_T^{(\text{free})} = 3/2$ as a function of lattice spacing calculated with our the model-averaged fit results for $f_{\sigma\sigma T}^2$ and Δ_T , as well as $\Delta_\sigma = 0.518(2)$ as obtained in [27]. (b) $C_T / C_T^{(\text{free})}$ multiplied by our model averaged fit results for $f_{\sigma\sigma\epsilon}^2 / \Delta_\epsilon^2$ as a function of the lattice spacing. For both quantities, we have performed extrapolations to $a/R \rightarrow 0$ according to (26) and (27) over different a/R -ranges. The extrapolations with the highest model probability (orange) are a linear extrapolation for $C_T / C_T^{(\text{free})}$ and a finite-size scaling based extrapolation for $C_T / C_T^{(\text{free})} \cdot f_{\sigma\sigma\epsilon}^2 / \Delta_\epsilon^2$, in both cases using all data points. The blue squares at $a/R = 0$ represent the continuum values obtained after model averaging all extrapolations. For comparison, the continuum bootstrap values are shown as dashed black lines.

$$G_\phi^{(2)}(t, \cos \theta) = \frac{2}{(2 \cosh t - 2 \cos \theta)^{\Delta_\sigma^{(\text{free})}}}, \quad (31)$$

where we now mean the primary operator σ of the free CFT for which $\Delta_\sigma^{(\text{free})} = 1/2$. The partial wave expansion Eq. (17) for the free theory then has the expansion coefficients

$$c_j^{(\text{free})}(t) = 8(2j+1) \sum_{n=0}^{\infty} e^{-(j+2n+1)t} \frac{2^j(j+n)!(2n-1)!!}{n!(2j+2n+1)!!}. \quad (32)$$

for the even j coefficients, while the odd j coefficients are zero. Moreover, as described in Appendix A, these equations may be modified to include the finite length (or finite temperature) of the cylinder.

We computed the four-point amplitude Eq. (30) on our lattices, replacing the free continuum propagator by the finite temperature lattice propagator, calculated by inverting the quadratic action numerically. The goal was then to analyze this synthetic free lattice data similarly to what was done for the interacting case, in order to study how well our lattices enable extrapolations to reproduce the exact free zero-temperature continuum OPE data in Eq. (32).

In particular, we calculated the finite temperature antipodal four-point function for the free theory for the lattice refinements $L \in \{4, 6, 8, 12, 16, 24, 32\}$ and different cylinder lengths L_t such that L_t/L was between 4 and 16. Projecting this data on the Legendre polynomials, we obtained the expansion coefficients $c_j^{(\text{free})}(t)$ for different values of L and L_t . The data for the different $c_j^{(\text{free})}(t)$ is also available in the Zenodo repository associated with this

project [44]. For the two coefficients with $j = 0$ and $j = 2$ also considered in the interacting theory, we then performed multiexponential fits of the form

$$c_j^{\text{fit}}(t) = \sum_k a_j^k (e^{-E_j^k t a_i/R} + e^{-E_j^k (L_t - t) a_i/R}) \quad (33)$$

in order to extract the leading coefficients and scaling exponents. In these fits, the finite temperature is only taken into account via the addition of the exponentials $e^{-E_k(L_t - t) a_i/R}$, just like it was done in the interacting theory. We then used a model-averaging procedure similar to what was described for the interacting theory in Sec. IV to average over fits to different t -ranges and, in this free case, different numbers of included exponentials.

Comparing Eq. (32) to Eq. (18), we can calculate the OPE coefficients $f_{\sigma\sigma\epsilon}^{(\text{free})}$ and $f_{\sigma\sigma T}^{(\text{free})}$ for the operators ϵ and T of the free CFT from the leading fit parameters a_j^0 and E_j^0 via

$$f_{\sigma\sigma\epsilon}^{(\text{free})2} = \frac{a_0^0}{4E_0^0} \\ f_{\sigma\sigma T}^{(\text{free})2} = \frac{3}{8 \cdot 4E_2^0} \left(a_2^0 - \frac{4E_0^0}{3(E_0^0 + 1)} a_0^0 \right). \quad (34)$$

Our lattice results for these OPE coefficients as well as the scaling dimensions $\Delta_\epsilon^{(\text{free})}$ and $\Delta_T^{(\text{free})}$ corresponding to the leading exponents in c_0 and c_2 , E_0^0 , and E_2^0 , respectively, can be seen in Fig. 9. We plot them as a function of $(\frac{a}{R})^2$, which we know to be the leading scaling behavior of lattice artifacts in the free case. The error bars stem from the fitting errors. Note that we do not show the results for $L = 4$ due to the fact that for such small lattice refinements, the fitting

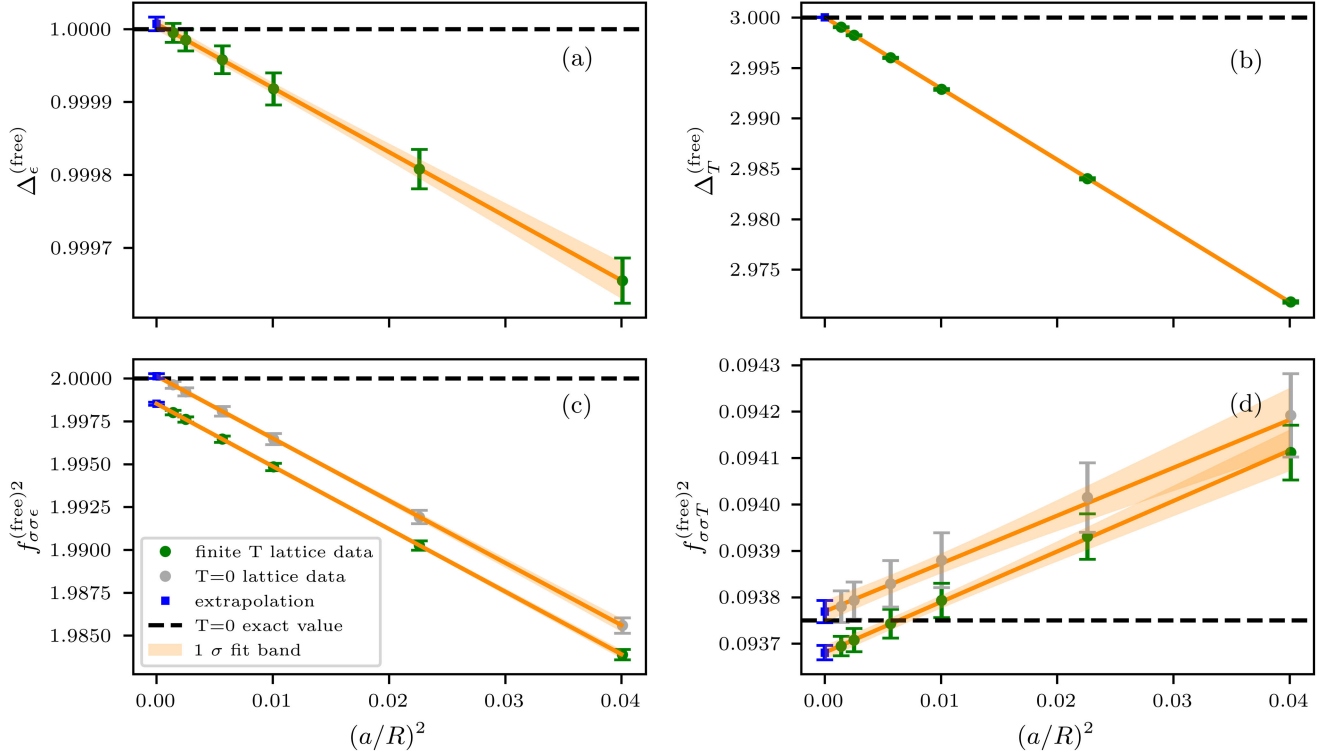


FIG. 9. Model-averaged fit results for the scaling dimensions and operator product expansion coefficients for the free operators ϵ (0^+) and T (2^+) as a function of the squared lattice spacing. The green results are taken at fixed finite temperature, $L_t/L = 16$, while the gray points in (c) and (d) are extrapolations to zero temperature $L_t/L \rightarrow \infty$. Extrapolations to the continuum (orange fit functions, blue squares at $a/R = 0$) are shown to compare with the exact continuum results at zero temperature (black dashed line).

errors are several orders of magnitudes higher than for the other refinements.

The results in green are taken at finite temperature with fixed $L_t/L = 16$ just as in the interacting theory. Extrapolating these to the continuum by fitting $f = c_0 + c_1(\frac{a}{R})^2$ leads to good agreement with the analytic values in the case of the scaling dimensions, which we expect to be $\Delta_\epsilon^{(\text{free})} = 1$ and $\Delta_T^{(\text{free})} = 3$ as $a/R \rightarrow 0$. The numerical values for these extrapolations are given in Table III.

The OPE coefficients, however, are affected by finite temperature effects. Thus, for the fixed finite ratio $L_t/L = 16$ corresponding to a finite temperature, the

TABLE III. Extrapolation results for the free theory compared to the zero-temperature exact values [compare Eq. (32)]. For the OPE coefficients $f_{\sigma\sigma\epsilon}^2$ and $f_{\sigma\sigma T}^2$ we list the continuum extrapolations obtained from the data with $L_t/L = 16$ fixed, as well as for data which had been extrapolated to zero temperature, $L_t/L \rightarrow \infty$, prior to the continuum extrapolation $a/R \rightarrow 0$.

Quantity	Exact value	$L_t/L = 16$	$L_t/L \rightarrow \infty$
$\Delta_\epsilon^{(\text{free})}$	1	1.0000073(94)	...
$\Delta_T^{(\text{free})}$	3	3.000030(35)	...
$f_{\sigma\sigma\epsilon}^{(\text{free})2}$	2	1.998527(93)	2.00014(15)
$f_{\sigma\sigma T}^{(\text{free})2}$	0.09375	0.093681(16)	0.093769(24)

extrapolations to $a/R \rightarrow 0$ with $f_{\sigma\sigma\epsilon}^{(\text{free})2} = 1.998527(93)$ and $f_{\sigma\sigma T}^{(\text{free})2} = 0.093681(16)$ slightly miss the zero temperature continuum expectations from Eq. (32) corresponding to $f_{\sigma\sigma\epsilon}^{(\text{free})2} = 2$ and $f_{\sigma\sigma T}^{(\text{free})2} = 0.09375$. However, these deviations due to wraparound effects only amount to 0.07%.

We can eliminate this systematic error by carrying out a double limiting procedure, first extrapolating the lattice results to zero temperature $L_t/L \rightarrow \infty$ via fit function $f(L_t) = f + p_1 e^{-p_2 L_t}$ for each L , yielding the gray data in Fig. 9, and then taking the limit $a \rightarrow 0$. Figure 9 and Table III show that if we perform this procedure, our results perfectly agree with the continuum zero temperature expectations.

From these results, we can draw two main conclusions. Firstly, as we know the scaling with the lattice spacing exactly, we can perfectly extrapolate the free theory data calculated on our simplicial lattices data to remove the IR and UV cutoff, yielding the free continuum values. This might be an incentive to study the cutoff dependence of the interacting theory to higher than just leading order in order to improve extrapolations.

Secondly, there are wraparound effects influencing our data if we only carry out calculations at finite T (finite L_t/L) and compare to $T \rightarrow 0$ ($L_t/L \rightarrow \infty$) continuum expectations. However, the errors associated with these

effects are around two orders of magnitude smaller than the deviations of our OPE coefficient results from the bootstrap values that we see in the interacting theory. Thus, we conclude that the improvement from carrying out a limit $L_1/L \rightarrow \infty$ in the interacting theory would be negligible compared to the effect of the systematic errors in the interacting theory that we could not study with the free case.

VII. CONCLUSION AND OUTLOOK

The quantum finite element program seeks to extend Euclidean Monte Carlo lattice methods to nonperturbative quantum field theory on curved manifolds. In particular, the present goal is to demonstrate its advantage when applied to radial quantization for $d \geq 3$ conformal field theory. For the prototype lattice ϕ^4 example, we have demonstrated that we can extract scaling dimensions and OPE coefficients for leading as well as subleading operators of the 3D Ising CFT from the four-point function on a $\mathbb{R} \times S^d$ manifold. In particular, this is the first time, to our knowledge, that the OPE coefficient $f_{\sigma\sigma T}$ has been determined from lattice Monte Carlo calculations.

Continuum extrapolations of our lattice simulations for the scaling dimensions of operators ϵ , T as well as the subleading operator ϵ' agree with the values obtained with the conformal bootstrap (and the exact value in the case of the energy-momentum tensor) within the statistical and fitting errors. Extrapolations for the OPE coefficients $f_{\sigma\sigma\epsilon}$ and $f_{\sigma\sigma T}$ deviate more from the bootstrap values than is covered by these errors so that also our value for the central charge is significantly too low in violation of the bootstrap lower bound [14]. However, ratios of these quantities extrapolate to values that are consistent with values obtained by the other two methods that were able to extract both $f_{\sigma\sigma\epsilon}$ and $f_{\sigma\sigma T}$, namely the conformal bootstrap and the fuzzy sphere, as is shown in the comparison Table IV.

The method employed here follows a sequence of quantum finite element developments. First, there is the requirement to introduce UV counterterms in 2D on S^2 and in 3D on $\mathbb{R} \times S^2$ to modify the simplicial finite element method (FEM) to reach the Ising critical surface. Next, the importance of the Ricci term in 3D was seen as it dramatically improved the approach to continuum for the scalar two-point function. While this simplicial QFE action has enabled us to study the OPE expansion, there are clearly additional improvements to pursue, as is common practice in lattice field theory.

TABLE IV. Comparison of the ratios obtained in this work with the corresponding values obtained with the conformal bootstrap [15,16] and the fuzzy sphere [31].

Quantity	This work	Bootstrap	Fuzzy sphere
$f_{\sigma\sigma\epsilon}^2/f_{\sigma\sigma T}^2$	10.30(16)	10.402(24)	10.53(23)
$C_T/C_T^{(\text{free})} \cdot f_{\sigma\sigma\epsilon}^2/\Delta_\epsilon^2$	0.528(16)	0.52478(13)	0.5310(86)

Comparison of the free scalar theory on the simplicial lattice vs the continuum free CFT reveals two issues. First, the finite temperature (also known as the IR finite length of the cylinder) is probably not a significant source of systematic error. Second, the extrapolation to zero lattice spacing (i.e. removing the UV cutoff) for the free CFT with $O(a^2)$ scaling is under good control. For the strongly interacting CFT, however, the analytic dependence on the cutoff is a more serious problem to address and finite-size scaling analysis offers some guidance.

Within the current QFE framework presented here, there are still some potential sources of systematic error that could be explored further. A slight mistuning of the bare mass parameter μ_0^2 could potentially lead to a systematic shift in estimated OPE coefficients. This can only be checked by new calculations at even larger values of L . Similarly, all calculations were performed at only a single bare λ_0 with no attempt to extrapolate to the bare lattice $\lambda_0 \rightarrow 0$. Also, our determinations of scaling dimensions and OPE coefficients were actually variational estimates limited by our inability to model the contributions of higher primaries: (ϵ'' , T'' , $\ell \geq 4$, etc.). Any of these studies would require a significant investment in software development for increased parallelization of the code as well as at least an order of magnitude increase in computational resources. Before making such an investment, we would like to consider whether this framework is the best option available.

Beyond cutoff effects, we continue to explore the validity of using perturbative counterterms in super-renormalizable theories. Recall that our counterterms only correct the mass parameter and do not modify the classical FEM Laplace-Beltrami operator [48,49] in Eq. (19). However, in a recent study of the 2D Ising model on an affine lattice [50], equivalent to lattice ϕ^4 at bare lattice $\lambda_0 \rightarrow \infty$, we demonstrated that the critical theory required a modification of the kinetic term away from the classical FEM operator. This provides yet further evidence that the way to continue using our current simplicial action in Eq. (21) with perturbative counterterms is to fix the dimensional renormalized coupling [$\lambda_R = \mathcal{O}(\lambda_0/a)$] instead of the bare λ_0 as we extrapolate to zero lattice spacing. This should reduce the quantum correction of FEM Laplace-Beltrami operator to $O(a)$.

ACKNOWLEDGMENTS

The authors are pleased to acknowledge that the computational work reported on in this paper was performed on the Shared Computing Cluster, which is administered by Boston University's Research Computing Services ([51]). We thank Casey Berger and Andrew D. Gasbarro, whose calculations this work builds upon. This work is supported by the U.S. Department of Energy (DOE) under Award No. DE-SC0019061 for G. T. F. (Yale), Award No. DE-SC0015845 for R. C. B., and Award No. DE-SC0019139 (E. K. O.) A. M. E. G. acknowledges support from Cusanuswerk Bischöfliche Studienförderung and the

Baden-Württemberg Stiftung. This document was prepared by the Quantum Finite Elements Collaboration using the resources of the Fermi National Accelerator Laboratory (Fermilab), a U.S. Department of Energy, Office of Science, Office of High Energy Physics HEP User Facility. Fermilab is managed by Fermi Research Alliance, LLC (FRA), acting under Contract No. DE-AC02-07CH11359.

APPENDIX A: THE FREE CASE

In the special case of the free theory, the propagator $G_\sigma^{(2)}(t, \cos \theta) \equiv \langle \sigma(t_1, \mathbf{n}_1) \sigma(t_2, \mathbf{n}_2) \rangle$ for a free scalar field $\sigma(t, \mathbf{n})$ on $\mathbb{R} \times S^2$ is

$$G_\sigma^{(2)}(t, \cos \theta) = \frac{2}{(2 \cosh t - 2 \cos \theta)^{\Delta_\sigma^{(\text{free})}}}, \quad (\text{A1})$$

where $t = |t_2 - t_1|$ and $\cos \theta = \mathbf{n}_1 \cdot \mathbf{n}_2$. Expanding as a series in Legendre polynomials this is

$$G_\sigma^{(2)}(t, \cos \theta) = \sum_{j=0}^{\infty} 2e^{-(j+1/2)t} P_j(\cos \theta), \quad (\text{A2})$$

where we have substituted the scaling exponent $\Delta_\sigma^{(\text{free})} = 1/2$.

The free antipodal four-point function is simply a sum of s -, t -, and u -channels. Following the same notation used above this gives

$$G_\sigma^{(4)}(t, \cos \theta) = G_\sigma^{(2)}(0, -1)^2 + G_\sigma^{(2)}(t, \cos \theta)^2 + G_\sigma^{(2)}(t, -\cos \theta)^2. \quad (\text{A3})$$

Note that we have conveniently normalized the two-point function (A2) so that the s -channel diagram is 1. Thus, the antipodal four-point function in this normalization already corresponds to the conformally invariant amplitude g . Inserting Eq. (A2) we obtain the somewhat complicated expression,

$$G_\sigma^{(4)}(t, \cos \theta) = 1 + 4 \left(\sum_{j=0}^{\infty} e^{-(j+1/2)t} P_j(\cos \theta) \right)^2 + 4 \left(\sum_{j=0}^{\infty} e^{-(j+1/2)t} P_j(-\cos \theta) \right)^2, \quad (\text{A4})$$

which can again be expressed as a series in Legendre polynomials

$$G_\sigma^{(4)}(t, \cos \theta) = 1 + \sum_{j=0}^{\infty} c_j^{(\text{free})}(t) P_j(\cos \theta), \quad (\text{A5})$$

where all of the odd j coefficients are zero, and the even j coefficients are

$$c_j^{(\text{free})}(t) = 8(2j+1) \sum_{n=0}^{\infty} e^{-(j+2n+1)t} \frac{2^j (j+n)! (2n-1)!!}{n! (2j+2n+1)!!}. \quad (\text{A6})$$

As required, we recover the partial wave expansion for a free scalar four-point function.

Finally, we consider corrections to (A5) due to wrap-around effects on a periodic cylinder with length L_t (i.e. finite temperature effects). In the free case, the thermal two-point function $\tilde{G}_\sigma^{(2)}$ in the interval $0 \leq t \leq L_t$ can be expressed as a sum over an infinite set of image charges,

$$\begin{aligned} \tilde{G}_\sigma^{(2)}(t, \cos \theta) &= \sum_{n=-\infty}^{\infty} G_\sigma^{(2)}(t + nL_t, \cos \theta) \\ &= 4 \sum_{j=0}^{\infty} \frac{\cosh [(\Delta_\sigma^{(\text{free})} + j)(t - L_t/2)]}{\sinh [(\Delta_\sigma^{(\text{free})} + j)L_t/2]} P_j(\cos \theta). \end{aligned} \quad (\text{A7})$$

The four-point function can be evaluated as before, and to lowest order, the finite temperature Legendre coefficients are related to the zero-temperature coefficients by $\tilde{c}_j^{(\text{free})}(t) \simeq c_j^{(\text{free})}(t) + c_j^{(\text{free})}(L_t - t)$. The leading corrections occur near $t = L_t/2$, giving

$$\delta \tilde{c}_0^{(\text{free})}(t \sim L_t/2) \simeq \frac{8}{\sinh(\Delta_\sigma^{(\text{free})} L_t/2)} \quad (\text{A8})$$

for $j = 0$ and

$$\delta \tilde{c}_j^{(\text{free})}(t \sim L_t/2) \simeq 16 \frac{\cosh [(\Delta_\sigma^{(\text{free})} + j - 1)(t - L_t/2)]}{\sinh [(\Delta_\sigma^{(\text{free})} + j)L_t/2]} \quad (\text{A9})$$

for all even $j \geq 2$.

APPENDIX B: FINITE-SIZE SCALING ANALYSIS FOR THE INTERACTING THEORY

To determine which fit function to use for extrapolating the lattice results to the continuum $a/R \rightarrow 0$, we carried out a finite-size scaling analysis based on [52].

1. Scaling of the free energy

The free energy is defined as

$$\mathcal{F}(g_\sigma, g_\epsilon, \{g_\omega, \dots\}, a/L) = \log Z, \quad (\text{B1})$$

where

$$Z = \int D\phi e^{-S+h\cdot\phi}. \quad (\text{B2})$$

Here, g_σ, g_ϵ are relevant and g_ω, \dots irrelevant couplings of the action near the Wilson-Fisher fixed point, not the bare couplings h, μ_0, λ_0 in the action. a is the lattice spacing, L is the characteristic ‘‘finite size’’ of our system, and a/L a dimensionless ratio.

If we change the scale by a factor λ , the free energy renormalizes as follows:

$$\begin{aligned} \mathcal{F}(g_\sigma, g_\epsilon, \{g_\omega, \dots\}, a/L) \\ = \lambda^{-d} F(\lambda^{y_\sigma} g_\sigma, \lambda^{y_\epsilon} g_\epsilon, \{\lambda^{y_\omega} g_\omega, \dots\}, \lambda a/L) \\ + G(g_\sigma, g_\epsilon). \end{aligned} \quad (\text{B3})$$

Here, F is the scaling part of \mathcal{F} , whereas G is regular. The exponents $y_\mathcal{O}$ are related to the scaling dimensions of the respective operators via $y_\mathcal{O} = d - \Delta_\mathcal{O}$.

2. n -point functions

We calculate connected n -point functions of the scalar field ϕ from \mathcal{F} by taking derivatives with respect to the (bare) external field h and subsequently setting $h = 0$:

$$\langle \phi(x_1) \cdots \phi(x_n) \rangle|_{\text{conn}} = \frac{\delta}{\delta h(x_1)} \cdots \frac{\delta}{\delta h(x_n)} \mathcal{F} \Big|_{h=0}. \quad (\text{B4})$$

Rewriting the derivatives with respect to g_σ , we get for the two-point function

$$\begin{aligned} \langle \phi(x_1) \phi(x_2) \rangle|_{\text{conn}} \\ = \int_{x,y} \frac{\delta^2 \mathcal{F}}{\delta g_\sigma(x) \delta g_\sigma(y)} \frac{\delta g_\sigma(x)}{\delta h(x_1)} \frac{\delta g_\sigma(y)}{\delta h(x_2)} \Big|_{h=0}, \end{aligned} \quad (\text{B5})$$

where we have used that g_σ is an odd function of h

$$g_\sigma = h\alpha_1 + h^3 \frac{\alpha_3}{3!} + h^5 \frac{\alpha_5}{5!} + \cdots \quad (\text{B6})$$

such that terms like $\frac{\delta^2 g_\sigma(x)}{\delta h(x_1) \delta h(x_2)}$ vanish. For the four-point function, we get

$$\begin{aligned} \langle \phi(x_1) \phi(x_2) \phi(x_3) \phi(x_4) \rangle|_{\text{conn}} = \int_{x,y,u,w} \frac{\delta^4 \mathcal{F}}{\delta g_\sigma(x) \delta g_\sigma(y) \delta g_\sigma(u) \delta g_\sigma(w)} \frac{\delta g_\sigma(x)}{\delta h(x_1)} \frac{\delta g_\sigma(y)}{\delta h(x_2)} \frac{\delta g_\sigma(u)}{\delta h(x_3)} \frac{\delta g_\sigma(w)}{\delta h(x_4)} \\ + \int_{x,y} \frac{\delta^2 \mathcal{F}}{\delta g_\sigma(x) \delta g_\sigma(y)} \left(\frac{\delta g_\sigma(x)}{\delta h(x_1)} \frac{\delta^3 g_\sigma(y)}{\delta h(x_2) \delta h(x_3) \delta h(x_4)} + \frac{\delta g_\sigma(x)}{\delta h(x_2)} \frac{\delta^3 g_\sigma(y)}{\delta h(x_1) \delta h(x_3) \delta h(x_4)} \right. \\ \left. + \frac{\delta g_\sigma(x)}{\delta h(x_3)} \frac{\delta^3 g_\sigma(y)}{\delta h(x_1) \delta h(x_2) \delta h(x_4)} + \frac{\delta g_\sigma(x)}{\delta h(x_4)} \frac{\delta^3 g_\sigma(y)}{\delta h(x_1) \delta h(x_2) \delta h(x_3)} \right). \end{aligned}$$

Derivatives of the free energy with respect to g_σ in the limit of $h \rightarrow 0$ and thus $g_\sigma \rightarrow 0$ scale as

$$\begin{aligned} \frac{\partial^k \mathcal{F}}{\partial g_\sigma^k} = \mathcal{F}^{(k)}(g_\epsilon, \{g_\omega, \dots\}, a/L) \\ = \left(\frac{L}{a}\right)^{ky_\sigma - d} F^{(k)}\left(\left(\frac{L}{a}\right)^{y_\epsilon} g_\epsilon, \left\{\left(\frac{L}{a}\right)^{y_\omega} g_\omega, \dots\right\}, 1\right) \\ + G^{(k)}(g_\epsilon). \end{aligned} \quad (\text{B7})$$

Near the critical point, we can expand these derivatives in Taylor series as follows:

$$\begin{aligned} F^{(k)} = a_{k0} + a_{k1}(g_\epsilon - g_\epsilon^*) \left(\frac{L}{a}\right)^{y_\epsilon} + a_{k2}(g_\epsilon - g_\epsilon^*)^2 \left(\frac{L}{a}\right)^{2y_\epsilon} + \cdots \\ + b_{k1}(g_\omega - g_\omega^*) \left(\frac{L}{a}\right)^{y_\omega} + b_{k2}(g_\omega - g_\omega^*)^2 \left(\frac{L}{a}\right)^{2y_\omega} + \cdots \end{aligned} \quad (\text{B8})$$

and

$$G^{(k)} = c_{k0} + c_{k1}(g_\epsilon - g_\epsilon^*) + c_{k2}(g_\epsilon - g_\epsilon^*)^2 + \cdots, \quad (\text{B9})$$

where g^* denotes the critical values of the couplings at the Wilson-Fisher fixed point.

Putting everything together, we see that the two-point function scales as

$$\langle \phi \phi \rangle|_{\text{conn}} \sim \left(\frac{L}{a}\right)^{2y_\sigma - 2d} \alpha_1^2 \left[F^{(2)} + \left(\frac{L}{a}\right)^{d-2y_\sigma} G^{(2)} \right] \quad (\text{B10})$$

near the critical point, whereas the connected four-point function scales as

$$\begin{aligned} \langle \phi \phi \phi \phi \rangle|_{\text{conn}} \sim \left(\frac{L}{a}\right)^{4y_\sigma - 4d} \alpha_1^4 \left[F^{(4)} + \left(\frac{L}{a}\right)^{d-4y_\sigma} G^{(4)} \right] \\ + 4 \left(\frac{L}{a}\right)^{2y_\sigma - 4d} \alpha_1 \alpha_3 \left[F^{(2)} + \left(\frac{L}{a}\right)^{d-2y_\sigma} G^{(2)} \right]. \end{aligned} \quad (\text{B11})$$

By tuning μ_0^2 in our action to the critical surface, we eliminate all terms $\propto (g_e - g_e^* = 0)$, which diverge as $L \rightarrow \infty$. The remaining terms then yield

$$\langle \phi \phi \rangle|_{\text{conn}} \sim \left(\frac{L}{a}\right)^{-2\Delta_\sigma} \alpha_1^2 \left[a_{20} + b_{21}(g_\omega - g_\omega^*) \left(\frac{L}{a}\right)^{d-\Delta_{\omega'}} + \dots \right. \\ \left. + \left(\frac{L}{a}\right)^{2\Delta_\sigma-d} c_{20} \right] \quad (\text{B12})$$

and

$$\langle \phi \phi \phi \phi \rangle|_{\text{conn}} \sim \left(\frac{L}{a}\right)^{-4\Delta_\sigma} \alpha_1^4 \left[a_{40} + b_{41}(g_\omega - g_\omega^*) \left(\frac{L}{a}\right)^{d-\Delta_{\omega'}} \right. \\ \left. + \dots + \left(\frac{L}{a}\right)^{-3d+4\Delta_\sigma} c_{40} \right] + 4 \left(\frac{L}{a}\right)^{-2\Delta_\sigma-2d} \alpha_1 \alpha_3 \\ \times \left[a_{20} + b_{21}(g_\omega - g_\omega^*) \left(\frac{L}{a}\right)^{d-\Delta_{\omega'}} + \dots \right. \\ \left. + \left(\frac{L}{a}\right)^{2\Delta_\sigma-d} c_{20} \right]. \quad (\text{B13})$$

We now have to take the ratio $\frac{\langle \phi \phi \phi \phi \rangle|_{\text{conn}}}{\langle \phi \phi \rangle \langle \phi \phi \rangle}$ of Eqs. (B13) and (B12) and expand in a/L . Using that for the $d=3$ Ising model, the leading irrelevant operator ω corresponds to the conformal primary ϵ' and comparing with the values for Δ_σ and $\Delta_{\epsilon'}$ in [15], we find that to leading order

$$\frac{\langle \phi \phi \phi \phi \rangle|_{\text{conn}}}{\langle \phi \phi \rangle \langle \phi \phi \rangle} = g(u, v) - 1 \\ \sim C_0 + C_1 \left(\frac{a}{R}\right)^{\Delta_{\epsilon'}-3} + \dots \quad (\text{B14})$$

such that the leading finite-size scaling exponent is $\Delta_{\epsilon'} - 3 \approx 0.83$. In our case, the characteristic ‘‘finite size’’ of our system is the radius of the sphere R . Thus, we expect the OPE coefficients from our fits at finite lattice spacing to receive corrections

$$f_{\sigma\sigma\mathcal{O}}^2 \left(\frac{a}{R}\right) = f_{\sigma\sigma\mathcal{O}}^2 + c'_{\mathcal{O}} \left(\frac{a}{R}\right)^{\Delta_{\epsilon'}-3} + \dots \quad (\text{B15})$$

to leading order. Taking the logarithm, we find that also

$$\Delta_{\mathcal{O}} \left(\frac{a}{R}\right) = \Delta_{\mathcal{O}} + c_{\mathcal{O}} \left(\frac{a}{R}\right)^{\Delta_{\epsilon'}-3} + \dots \quad (\text{B16})$$

Note, C_1 in Eq. (B14) as the leading correction to scaling is a function of the irrelevant couplings and its value can be set to zero by tuning the bare couplings [53], thereby increasing the rate of convergence of the discrete theory to the continuum limit. This is often referred to as non-perturbative improvement of the discrete action.

-
- [1] T. Andrews, The Bakerian lecture: On the continuity of the gaseous and liquid states of matter, *Phil. Trans. R. Soc. London* **159**, 575 (1869).
- [2] K. G. Wilson, Renormalization group and critical phenomena. I. Renormalization group and the Kadanoff scaling picture, *Phys. Rev. B* **4**, 3174 (1971).
- [3] A. Parola and L. Reatto, Liquid state theories and critical phenomena, *Adv. Phys.* **44**, 211 (1995).
- [4] M. Anisimov, *Critical Phenomena in Liquids and Liquid Crystals* (Gordon and Breach Science Publishers, New York, 1991).
- [5] A. Pelissetto and E. Vicari, Critical phenomena and renormalization group theory, *Phys. Rep.* **368**, 549 (2002).
- [6] R. H. Swendsen and J.-S. Wang, Nonuniversal critical dynamics in Monte Carlo simulations, *Phys. Rev. Lett.* **58**, 86 (1987).
- [7] U. Wolff, Collective Monte Carlo updating for spin systems, *Phys. Rev. Lett.* **62**, 361 (1989).
- [8] M. Hasenbusch, Finite size scaling study of lattice models in the three-dimensional Ising universality class, *Phys. Rev. B* **82**, 174433 (2010).
- [9] M. Hasenbusch, Restoring isotropy in a three-dimensional lattice model: The Ising universality class, *Phys. Rev. B* **104**, 014426 (2021).
- [10] A. M. Polyakov, Conformal symmetry of critical fluctuations, *JETP Lett.* **12**, 381 (1970), http://jetpletters.ru/ps/1737/article_26381.shtml.
- [11] S. Rychkov, 3d Ising model and conformal bootstrap (2013), CERN Winter School on Supergravity, Strings, and Gauge Theory.
- [12] S. Rychkov, Conformal bootstrap in three dimensions?, [arXiv:1111.2115](https://arxiv.org/abs/1111.2115).
- [13] S. El-Showk, M. F. Paulos, D. Poland, S. Rychkov, D. Simmons-Duffin, and A. Vichi, Solving the 3d Ising model with the conformal bootstrap, *Phys. Rev. D* **86**, 025022 (2012).
- [14] S. El-Showk, M. F. Paulos, D. Poland, S. Rychkov, D. Simmons-Duffin, and A. Vichi, Solving the 3d Ising model with the conformal bootstrap II. C-minimization and precise critical exponents, *J. Stat. Phys.* **157**, 869 (2014).
- [15] D. Simmons-Duffin, The lightcone bootstrap and the spectrum of the 3d Ising CFT, *J. High Energy Phys.* **03** (2017) 086.
- [16] M. Reehorst, Rigorous bounds on irrelevant operators in the 3d Ising model CFT, *J. High Energy Phys.* **09** (2022) 177.
- [17] F. Rose, C. Pagani, and N. Dupuis, Operator product expansion coefficients from the nonperturbative functional renormalization group, *Phys. Rev. D* **105**, 065020 (2022).

- [18] M. Hasenbusch, Two- and three-point functions at criticality: Monte Carlo simulations of the improved three-dimensional Blume-Capel model, *Phys. Rev. E* **97**, 012119 (2018).
- [19] V. Herdeiro, Numerical estimation of structure constants in the three-dimensional Ising conformal field theory through Markov Chain UV sampler, *Phys. Rev. E* **96**, 033301 (2017).
- [20] M. Caselle, G. Costagliola, and N. Magnoli, Numerical determination of the operator-product-expansion coefficients in the 3d Ising model from off-critical correlators, *Phys. Rev. D* **91**, 061901(R) (2015).
- [21] G. Costagliola, Operator product expansion coefficients of the 3d Ising model with a trapping potential, *Phys. Rev. D* **93**, 066008 (2016).
- [22] J.L. Cardy, Universal amplitudes in finite-size scaling: Generalisation to arbitrary dimensionality, *J. Phys. A* **18**, L757 (1985).
- [23] S. Fubini, A. J. Hanson, and R. Jackiw, New approach to field theory, *Phys. Rev. D* **7**, 1732 (1973).
- [24] R. C. Brower, G. Fleming, A. Gasbarro, T. Raben, C.-I. Tan, and E. Weinberg, Quantum finite elements for lattice field theory, *Proc. Sci. LATTICE2015* (2016) 296. [arXiv:1601.01367].
- [25] R. C. Brower, M. Cheng, E. S. Weinberg, G. T. Fleming, A. D. Gasbarro, T. G. Raben, and C.-I. Tan, Lattice ϕ^4 field theory on Riemann manifolds: Numerical tests for the 2-d Ising CFT on \mathbb{S}^2 , *Phys. Rev. D* **98**, 014502 (2018).
- [26] R. C. Brower, E. S. Weinberg, G. T. Fleming, A. D. Gasbarro, T. G. Raben, and C.-I. Tan, Lattice Dirac fermions on a simplicial Riemannian manifold, *Phys. Rev. D* **95**, 114510 (2017).
- [27] R. C. Brower, G. T. Fleming, A. D. Gasbarro, D. Howarth, T. G. Raben, C.-I. Tan, and E. S. Weinberg, Radial lattice quantization of 3D ϕ^4 field theory, *Phys. Rev. D* **104**, 094502 (2021).
- [28] S. Rychkov, D. Simmons-Duffin, and B. Zan, Non-gaussianity of the critical 3d Ising model, *SciPost Phys.* **2**, 001 (2017).
- [29] A.-M. E. Glück, G. T. Fleming, R. C. Brower, V. Ayyar, E. K. Owen, T. G. Raben, and C.-I. Tan, Computing the central charge of the 3d Ising CFT using quantum finite elements, *Proc. Sci. LATTICE2022* (2023) 370.
- [30] C. Han, L. Hu, W. Zhu, and Y.-C. He, Conformal four-point correlators of the 3d Ising transition via the quantum fuzzy sphere, *Phys. Rev. B* **108**, 235123 (2023).
- [31] L. Hu, Y.-C. He, and W. Zhu, Operator product expansion coefficients of the 3d Ising criticality via quantum fuzzy spheres, *Phys. Rev. Lett.* **131**, 031601 (2023).
- [32] P. Di Francesco, P. Mathieu, and D. Senechal, *Conformal Field Theory*, Graduate Texts in Contemporary Physics (Springer-Verlag, New York, 1997).
- [33] S. Rychkov, EPFL lectures on conformal field theory in $D \geq 3$ dimensions, arXiv:1601.05000.
- [34] F. A. Dolan and H. Osborn, Conformal four point functions and the operator product expansion, *Nucl. Phys.* **B599**, 459 (2001).
- [35] F. A. Dolan and H. Osborn, Conformal partial waves: Further mathematical results, arXiv:1108.6194.
- [36] M. Hogervorst and S. Rychkov, Radial coordinates for conformal blocks, *Phys. Rev. D* **87**, 106004 (2013).
- [37] M. S. Costa, T. Hansen, J. a. Penedones, and E. Trevisani, Radial expansion for spinning conformal blocks, *J. High Energy Phys.* **07** (2016) 057.
- [38] R. C. Brower and P. Tamayo, Embedded dynamics for ϕ^4 theory, *Phys. Rev. Lett.* **62**, 1087 (1989).
- [39] N. Metropolis, A. W. Rosenbluth, M. N. Rosenbluth, A. H. Teller, and E. Teller, Equation of state calculations by fast computing machines, *J. Chem. Phys.* **21**, 1087 (1953).
- [40] S. L. Adler, An overrelaxation method for the Monte Carlo evaluation of the partition function for multiquadratic actions, *Phys. Rev. D* **23**, 2901 (1981).
- [41] C. Whitmer, Overrelaxation methods for Monte Carlo simulations of quadratic and multiquadratic actions, *Phys. Rev. D* **29**, 306 (1984).
- [42] F. R. Brown and T. J. Woch, Overrelaxed heat bath and metropolis algorithms for accelerating pure gauge Monte Carlo calculations, *Phys. Rev. Lett.* **58**, 2394 (1987).
- [43] M. Creutz, Overrelaxation and Monte Carlo simulation, *Phys. Rev. D* **36**, 515 (1987).
- [44] A.-M. E. Glück, V. Ayyar, R. C. Brower, G. T. Fleming, E. K. Owen, T. G. Raben, and C.-I. Tan, Dataset for “The operator product expansion for radial lattice quantization of 3D ϕ^4 theory” (2023), <https://doi.org/10.5281/zenodo.10039534>.
- [45] W. I. Jay and E. T. Neil, Bayesian model averaging for analysis of lattice field theory results, *Phys. Rev. D* **103**, 114502 (2021).
- [46] R. H. Byrd, P. Lu, J. Nocedal, and C. Zhu, A limited memory algorithm for bound constrained optimization, *SIAM J. Sci. Comput.* **16**, 1190 (1995).
- [47] For $L = 36$ some of the most probable fits had unphysical values of $\Delta_{\mathcal{E}} < \Delta_{\mathcal{T}}$, which we discarded.
- [48] G. Strang and G. Fix, *An Analysis of the Finite Element Method*, 2nd ed. (Wellesley-Cambridge, Wellesley, MA, 2008).
- [49] M. Desbrun, A. N. Hirani, M. Leok, and J. E. Marsden, Discrete exterior calculus, arXiv:math/0508341.
- [50] R. C. Brower and E. K. Owen, Ising model on the affine plane, *Phys. Rev. D* **108**, 014511 (2023).
- [51] www.bu.edu/tech/support/research/.
- [52] H. W. J. Blote, E. Luijten, and J. R. Heringa, Ising universality in three dimensions: A Monte Carlo study, *J. Phys. A* **28**, 6289 (1995).
- [53] M. Hasenbusch, K. Pinn, and S. Vinti, Critical exponents of the three-dimensional Ising universality class from finite-size scaling with standard and improved actions, *Phys. Rev. B* **59**, 11471 (1999).